ACS APPLIED ELECTRONIC MATERIALS

Article

Cite This: ACS Appl. Electron. Mater. 2019, 1, 1198−1207

pubs.acs.org/acsaelm

New Opportunities in Metallization Integration in Cofired Electroceramic Multilayers by the Cold Sintering Process

Thomas Hérisson de Beauvoir, Sinan Dursun,* Lisheng Gao, and Clive Randall

Materials Research Institute, Department of Material Science and Engineering, The Pennsylvania State University, University Park, Pennsylvania 16802, United States

Supporting Information

ABSTRACT: Metallization with high conductivities is critical in the design of high performance multilayer electroceramic devices. Cold sintering offers exciting new opportunities in the integration of different material classes; here we explore novel metal chemistries and demonstrate their integration into ceramic multilayers. The processing is enabled due to the cosintering of both the ceramic and metal powders in fast times and at extremely low sintering temperatures. Metal powders are printed as pastes and formed into multilayers that can be cosintered with the ceramic ZnO; these specific metals include Cu, Fe, and Al. The multilayer structures are assembled and fabricated under a thick film process and enabled by using a polypropylene carbonate binder system that can be removed at low temperatures under N_2−H_2 forming gas, permitting control of oxidation of the Cu, Fe, and Al. As a result, extremely high conductivity electrodes are fabricated and quantified through the equivalent series resistance (ESR). In addition, new electrode composite concepts, such as mixed particles of Fe−Cu cosintered in between the ZnO layers, are possible with the cold sintering process.

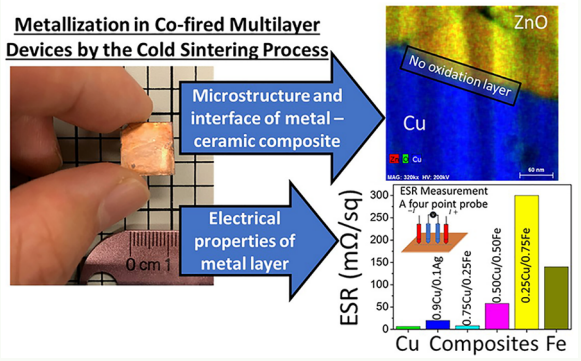

KEYWORDS: *cold sintering, metallization, cofiring, electroceramic multilayers, zinc oxide*

INTRODUCTION

In the thick film production of multilayer ceramic capacitors (MLCCs), there has been a remarkable increase in volumetric capacitive efficiency over the past 15−20 years. To enable this, there has been size reduction of the thicknesses of both the electrodes and dielectric layers; at this time, the state-of-the-art is driving these dimensions to below 0.5 μm while still maintaining high reliability and yield in production.[1,2] The selection of base metal electrodes and/or high silver alloys has been a major cost savings relative to the earlier technologies that used Pt and/or Pd electrodes, and now base metal chemistries dominate the metallization of choice with over 90% in the overall 3 trillion MLCC devices manufactured annually.

There are many other examples of multilayer electroceramic components and devices. These applications range from capacitors, varistors, positive temperature coefficient resistors (PTCR), negative temperature coefficient (NTC) thermistors, inductors, piezoelectric transformers, actuators, electrocaloric cooling systems, Li batteries, chemical sensors, microwave filters, antennas, electronic packages, thermoelectrics, and oxygen and planar solid oxide fuel cells.[3−19] Table 1 summarizes the variety of basic materials and the metals that are used in the multilayers. In all these applications, the metallization function is to provide an embedded conductive pathway on a layer to control/sense the electrical potential around a nonmetal electroceramic material.

The fabrication of multilayer devices uses controlled tape casting and/or screen-printing processes.[20,21] Details of this production method can be found elsewhere which covers many important details in the engineering of the tapes, powders, inks and their printing, drying, and lamination.[22] The basic operations under this process are summarized in Figure 1. There are many different organic materials that can be blended in the formation of slurries and pastes to allow dispersion, dimensional stability of the tape under the rheological process of casting, adhesion on lamination, printability, and the ability to have enough strength in the handling and stacking process. A clean binder removal that provides low residual carbon and no-crack formation under the polymer decomposition, the thermal profiles, and the kinetics of the decomposition processes are all important.[23,24]

Additional defects in the cofiring process of multilayer electroceramics arise from differential shrinkage rates between the electrode layer and the respective ceramic layers.[40−44] These create stresses that can lead to physical flaws in the multilayers, such as warpages, cracking, and porosity. There are also other concerns regarding the metallization in a cofired electroceramic. For example, there can be a vapor transport into the ceramic grain boundaries under the sintering process,

Received: March 20, 2019
Accepted: June 24, 2019
Published: June 24, 2019

DOI: 10.1021/acsaelm.9b00184
ACS Appl. Electron. Mater. 2019, 1, 1198−1207

Table 1. Summary of the Various Metallization in Multilayer Electroceramic Components and Devices

application/device	electroceramic material	cofired metallized electrode	ref
ceramic capacitor	$BaTiO_3$, $Ca(Zr,Ti)O_3$, $PbZrO_3$,$BaTiO_3$−$Bi(Mg_{0.5}Ti_{0.5})O_3$, $BiScO_3$−$Pb(Mg_{1/3}Nb_{2/3})O_3$−$PbTiO_3$	Pt, Pd, Ag−Pd, Ag, Ni, Cu	1, 24−26
negative temperature coefficient resistor (NTC)	$NiMn_2O_4$	Ag−Pd	5
positive temperature coefficient thermistor (PTCR)	$BaTiO_3$, $(K,Bi)TiO_3$	Pt, Ni	27−29
magnetic inductors/filters	$(Ni,Zn)Fe_2O_4$	Ag	10
piezoelectric transformers	$Pb(Zr,Ti)O_3$, $Pb(Mg_{1/3}Nb_{2/3})O_3$−$PbTiO_3$	Pt, Ag, Ag−Pd, Cu	7, 8
piezoelectric actuators	$Pb(Zr,Ti)O_3$, $(Na,K)NbO_3$	Pt, Ag−Pd, Cu	9, 29−34
multilayer Li batteries	$LiNiO_2$ (anodes/cathodes)	Ag	35
microwave LTCC filters/antennas	alumina-filled glass ceramics	Ag, Cu, Au, Al	14, 36, 37
solid oxide fuel cell	ZrO_2	Ni cermet	19
laminar oxygen sensors	ZrO_2	Pt	38
multilayer varistors	ZnO	Pt, Ag−Pt, Ag−Pd	39

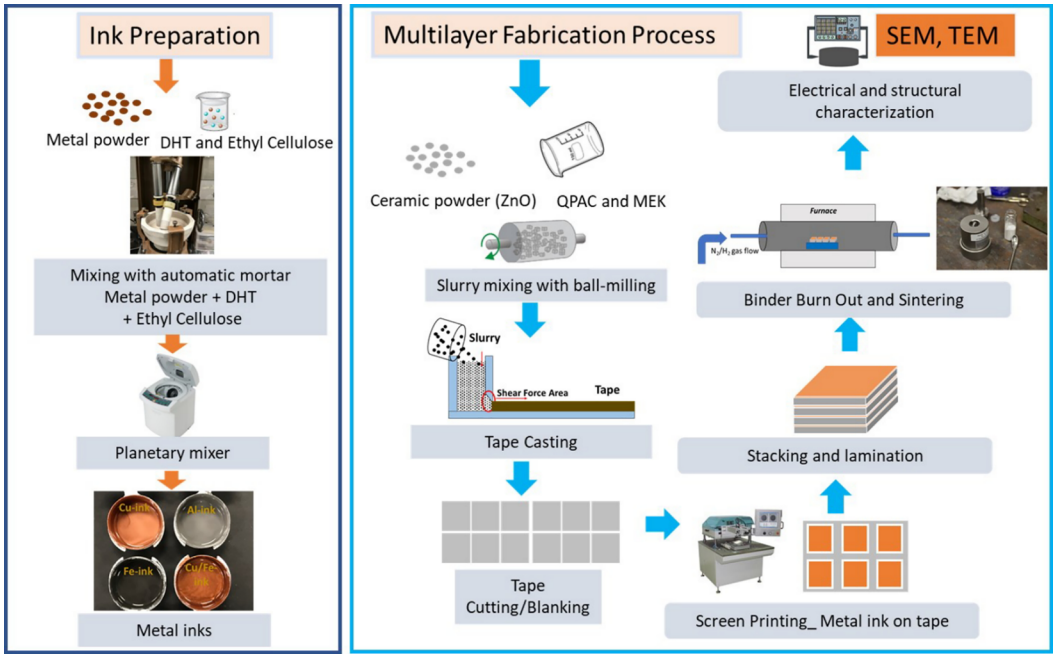

Figure 1. Schematic representation of metallization integration in cofired multilayer electroceramic devices.

and these metal ions can, under electrical bias and humidity, migrate and create dendrites along the grain boundaries. This drives short circuits across capacitive layers and failure of the device. Such problems can exist with Ag electrodes in dielectrics and piezoelectrics.[33,45,46] In the case of Ag−Pd alloy metallization, there can also be a segregation, with the Pd undergoing an oxidation, and this can, under binder removal and heating in the sintering process, both increase in volume and then later shrink. In both cases, this propagates stresses and creates a delamination in the firing of the multilayers.[34] Details of this type of mechanism and the associated strain problems in AgPd electrodes have been investigated by Wang et al. and others.[47,48] In other examples, the electrode interface with the semiconducting oxide material may have to be designed to provide electrical stable contacts. In the case of thermistors, such as NTC and PTCR, the electrode−semiconductor interfaces must be the ohmic contacts and remain stable with no drift in contact resistance over the lifetime of the device. In multilayer ceramic capacitors, nickel and copper have become the dominant electrode materials in the production of these so-called base-metal electrodes. The control of reduction and oxidation under the thermal processing is critical in the design of successful devices, in terms of both the ceramic and the interconnected metal electrode system. This controls both the roughness of electrodes and the interfacial Schottky barriers, aiding high insulation resistance.

In the case of cold sintering, many new opportunities are there to integrate many types of materials.[49−54] Cold sintering uses a transient phase that enables sintering at extremely low temperatures below 300 °C and under uniaxial pressure with pressures from 100 up to 500 MPa. This has been termed the "cold sintering process", and it has broad applications across many different ceramic materials and composites; in the case of electroceramic devices, the ability to integrate and cosinter electrodes under such conditions will be essential as this technology evolves.

The objective of this paper is to demonstrate the broad number of metallizations that can be integrated into multilayer electroceramics via cold sintering. Here we will focus on a

DOI: 10.1021/acsaelm.9b00184
ACS Appl. Electron. Mater. 2019, 1, 1198−1207

model ZnO ceramic, develop a multilayer process, and access the microstructural development and the associated control of oxidation as well as the resulting conductivity in terms of the equivalent series resistance.

EXPERIMENTAL SECTION

Figure 1 shows the simplified schematic representation of the tape, ink, and multilayer fabrication steps. To prepare prototypes for the multilayer devices, we used different metal inks, Cu, Fe, Al, and mixed Fe/Cu and selected a commercially available ZnO powder (Alfa Aesar, nanopowder, 99+% (metals basis), CAS: 1314-13-2) for tape preparation. The tape cast slurries were prepared from ZnO powder and polypropylene carbonate (PPC) (QPAC-40, Empower Materials, New Castle, DE). The tape casting slurry was prepared in MEK by ball milling for 24 h. Details of binder and slurry preparation can be found elsewhere.[31] The slurry mixture was placed in a planetary mixer to further mix and remove foam from slurry before casting. Slurries were cast on a thick film with constant rate of doctor blade through casting direction. Then they were dried and cut into 0.5 in. (12.7 mm) squares.

Metal inks (or electrodes) were prepared by mixing metal powders of iron (Fe) (Alfa-Aesar), copper (Cu) (SHOEI Chemical Inc. Japan), aluminum (Al) (Ferro-Corporation), and a composite mixture of Fe/Cu powders with dihydroterpineol (DHT, Alfa Aesar) and ethyl cellulose. The metal powders and polymers were first mixed by using an automatic mortar and pestle, which provides a high shear mixing of the paste; then this is transferred into a planetary mixer (see Figure 1 in ink preparation). Metal electrodes were screen printed from the pastes into patterns on half-inch ZnO square tapes. Then printed tapes were stacked alternately, and immediately afterward, they were pressed lightly in a uniaxial press at 75 °C to improve the stability of the multilayer before lamination. Stacked printed tapes were laminated (IL4004, Pacific Trinetics Co., San Marcos, CA) at 75 °C under 3000 psi for 30 min. Each laminated multilayer sample was then thermally treated for binder burnout (BBO). BBO was performed at 250 °C for 3 h with a slow heating rate (0.5 °C/min) in a H_2(5 vol %)/N_2(95 vol %) forming gas flowing atmosphere. Binder-free multilayer samples were hooked in a beaker and stirred in 2 M acetic acid aqueous solution at 85 °C for 1 h. After humidification, samples were placed in stainless steel 0.5 in. square die and uniaxially pressed at 200 MPa. The die was heated to 260 °C and held for 1 h under the same pressure condition. Eventually, the pressure was released, and the die was left to cool. Multilayer samples were taken out from the cooled die, and then electrical and structural characterizations were carried out.

Electrical sheet resistance (ESR) was used to characterize on top metal electrode materials of multilayer samples. ESR is performed by using four electrical probes in a line with the same length (L) between each of probes as sketched in Figure 2. The current of the first probe is passed through to probe 4, while an induced voltage is measured between the inner voltage probes (probes 2 and 3). The sheet resistance is calculated by using eq 1:

$$R_{\text{sheet resistance}} = \frac{\pi}{\ln(2)}\frac{\Delta V}{I}(G) \quad (1)$$

Although the unit of eq 1 is ohm (Ω), an alternative to the common unit is ohms per square (Ω/sq), which represents the resistance between opposite sides of a square and dimensionally equivalent to an ohm used solely in the context of sheet resistance. The geometric correction factor (G) only can be used when the sample dimensions are significantly larger than the distance between probes. In our case, the half-inch square multilayer sample shown in Figure 2 has an edge of W = 12.7 mm and the spacing of the probes is L = 1.3 mm; as such, the geometric correction factor of our samples is 0.9313.[55]

X-ray diffraction (PANalytical Empyrean system) with Cu $K\alpha_1$ radiation was performed on multilayer surface after binder burnout and after sintering to identify phase composition, thereby revealing the oxidation present on a metal powder (before sintering) and electrode (after sintering). A schematic representation of the XRD measurement is given in Figure S1. Microstructures of samples were observed with a scanning electron microscope (SEM), and chemical mapping was performed with energy dispersive spectroscopy (EDS) (SEM, FEI Q250), both electrode and ceramic layers. Furthermore, to understand the interface diffusion, oxidation, and structure between the metal/metal, metal/ceramic, and ceramic/ceramic grains, high-resolution transmission electron microscopy (FEI Talos, F200X, Eindhoven, Netherlands) and energy dispersive spectroscopy (EDS) mapping were performed by using a SuperX EDS by the scanning transmission electron microscopy (STEM) mode using a high angle annular dark field (HAADF) detector.

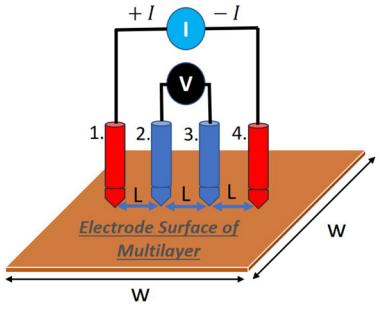

Figure 2. Schematic representation of ESR measurement that consists of four-point probes in contact with the electrode surface of multilayer, having identical spacing (L). A current (I) flows through probe 1 and is collected at probe 4; the voltage is concurrently measured between probes 2 and 3.

RESULTS AND DISCUSSION

To achieve preparation and densification of particulates into dense and functional multilayered structures, two different thermal processing treatments are applied. The first consists of a thermal binder burnout, and the second is the sintering step. It should be noted that Cu, Fe, and Al metals are easily oxidized, even at a temperature around 150 °C under ambient conditions.[56−59] Therefore, temperature and atmosphere are critical parameters in this debinding process, and yet the temperatures must be high enough to allow total decomposition and transport of binder out from the formed parts but also low enough temperature to avoid metal oxidation.[60,61] Hence, polypropylene carbonate (PPC, QPAC-40, Empower Materials, New Castle, DE) was chosen as a binder system. We performed the thermogravimetric analysis (TGA) measurement at different temperatures to demonstrate the PPC-based binder complete removal from the system. Figure 3 shows a thermogravimetric analysis (TGA) of ZnO tape prepared by using polypropylene carbonate binder systems at different temperatures, ranging from 100 to 150 °C, using a 12 h dwell time, under a nitrogen atmospheres. It is important to notice the total binder removal at 150 °C after 4 h, as 14.0 wt % loss is reached, corresponding to mass loss measured on ZnO tape treated overnight at 250 °C. Binder removal can also be achieved at lower temperatures by increasing the soaking time; for example, at 125 °C, almost complete binder removal is achieved after 12 h of heat treatment. In the case of the 100 °C treatment, 10.2 wt % loss is observed after 12 h, which corresponds to 73 wt % of total binder quantity. It is also visible that mass loss is not complete after these 12 h at 100 °C, suggesting that it would be possible to further improve it by increasing soaking time. In the present work, however, it is not necessary to decrease temperature as low as 100 °C, since burnout can also be achieved under vacuum at 250 °C,

DOI: 10.1021/acsaelm.9b00184
ACS Appl. Electron. Mater. 2019, 1, 1198−1207

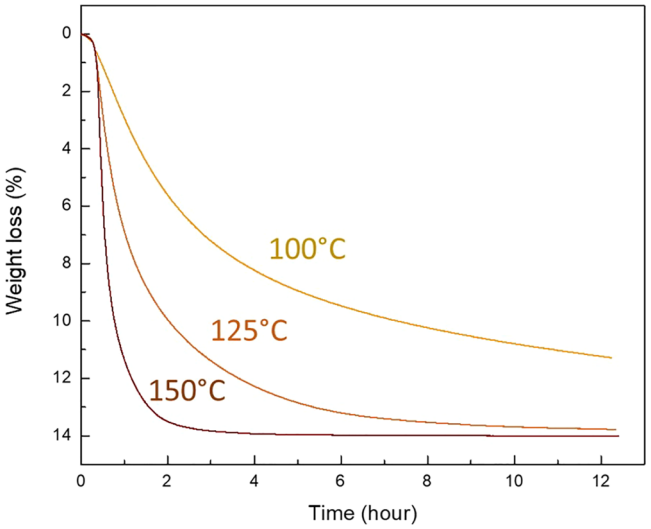

Figure 3. TGA under nitrogen at various temperatures on ZnO tapes. The thermal ramp is set to 5 °C/min and the soaking time to 12 h.

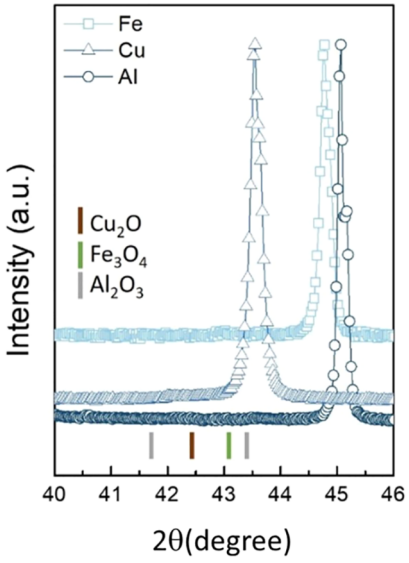

Figure 4. XRD plots of ZnO−Cu, ZnO−Al, and ZnO−Fe samples after cold sintering. Their corresponding oxide peak positions are represented by brown (Cu_2O), green (Fe_3O_4), and gray (Al_2O_3) bars.

allowing total binder decomposition. The PPC-based binder system has burnout efficiency as good, or better, than other binder materials such as PVB/PVA or ethyl cellulose at relatively low temperatures. In contrast to QPAC, PVB/PVA or ethyl cellulose binder systems need to be firing at around 500 °C to removal the organic binders; moreover, it was demonstrated that a detectable residual carbon was found even if at 1000 °C in the N_2 atmosphere.[62−64] Furthermore, the PPC binder system was demonstrated as an ideal binder system for Cu and Ni metallization in multilayer ceramic capacitors (MLCC) and low-temperature cofired ceramic (LTCC) processing.[31] Additionally, further proof of the clean burnout of PPC binder is given by the lack of a residual carbon signal after sintering (STEM-EDS analysis, Figures 7 and 8). It is shown that the BBO is performed effectively with the use of the PPC binder system under the H_2/N_2 condition. This result enables a new opportunity in low-temperature processing of multilayer devices, since it opens possibilities in integrating and forming low-temperature stability materials, such as polymers, in ceramic-containing composites.

The second temperature treatment applied is the sintering itself; with cold sintering strategies, this can be achieved at 260 °C in ambient atmosphere in a die. In that case, it is important to realize that the sample is pressed in a die, which limits contact with air. However, the system is not sealed, so metal oxidation remains possible. After sintering, to access the control of metal oxidation during sintering step, an XRD analysis is performed on all samples as an initial check (Figure S2). Figure 4 shows XRD diffractograms at the vicinity of metal peak position. Bragg reflection positions of corresponding oxides are marked for each sample. According to XRD results, no large oxidation can be evidenced along the sintering step, confirming stability of the materials through the two thermal treatments. After BBO and sintering, XRD data of the samples for the 2θ for the 30°−60° angle range can be seen in Figures S2 and S3, respectively.

After confirmation of metallic phase purity by the XRD, samples were observed by using SEM to control both their microstructure and characterize cationic position using EDX analysis. Figure 5 shows microstructures of the three different samples containing Cu, Fe, and Al. The various metal powders used have different particle size and shape, which is observed on the resulting materials. While Fe and Cu grain sizes range from 2 to 5 μm, Al grains are larger, with a grain size between 5 and 10 μm. The ZnO layers were prepared the same way for each sample, resulting in a coherent layer thickness of ∼20 μm. The ZnO microstructure is displayed in Figure 6f, showing prismatic and highly dense microstructure, with no visible porosity remaining after the cold sintering. These observations correspond well to previous work done on bulk ZnO,[53] showing almost complete densification in the presence of acetic acid and water at temperatures as low as 250 °C.

It is important that the metals also show compatibility with the dense microstructures of ZnO ceramics and at the controlled interfaces between the layers. To check whether chemically graded interfaces occur with metal diffusion into ceramic region, or vice versa, EDS mapping was performed. All layers remain parallel to each other, with similar thicknesses across the samples, and no evidence of delamination at the interface was found. The cold sintering achieves densification of both the zinc oxide and the metallic layer while avoiding interdiffusion. Although the metal particles exhibit some porosity due to the exceedingly low sintering temperature, the formation of necks occurs between metal grains during cold sintering, as can be seen from the micrographs in Figure 5. Also, the effect of humidity on device performance should be considered. This is shown in Figure 5a−c; we observe that architectural design of the multilayers is preserved throughout the all preparation processes. It is interesting that contrary to the Cu and Al electrode layers, ZnO grains appear to intrude into the Fe electrodes, as shown in Figure 5e. In fact, the intrusion of ceramic or metal grains can be attributed to the processing stage during printing, stacking or lamination of the multilayer, or metal ink preparation during the experimental steps outlined in Figure 1. The state-of-art processing will ensure the continuous metal/ceramic layer to prevent any incursion of layers in future work. Line profiling with EDS scans (Figure 5g−i) was performed orthogonal to the metallic−ceramic layers and confirm clean interfaces with the absence of long-range cationic diffusion between adjacent

DOI: 10.1021/acsaelm.9b00184
ACS Appl. Electron. Mater. 2019, 1, 1198−1207

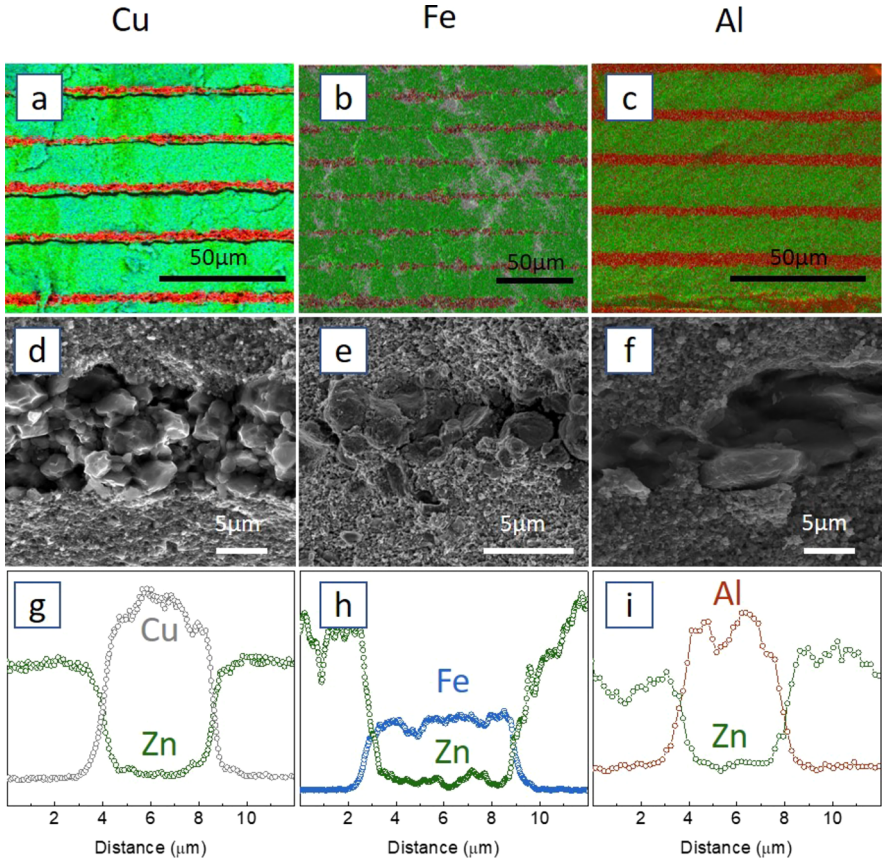

Figure 5. (a–c) SEM–EDX mapping, (d–f) SEM zoom-in image of the interface region, and (g–i) EDX line scan across the metallic layer of ZnO–M (M = Cu, Fe, Al) samples.

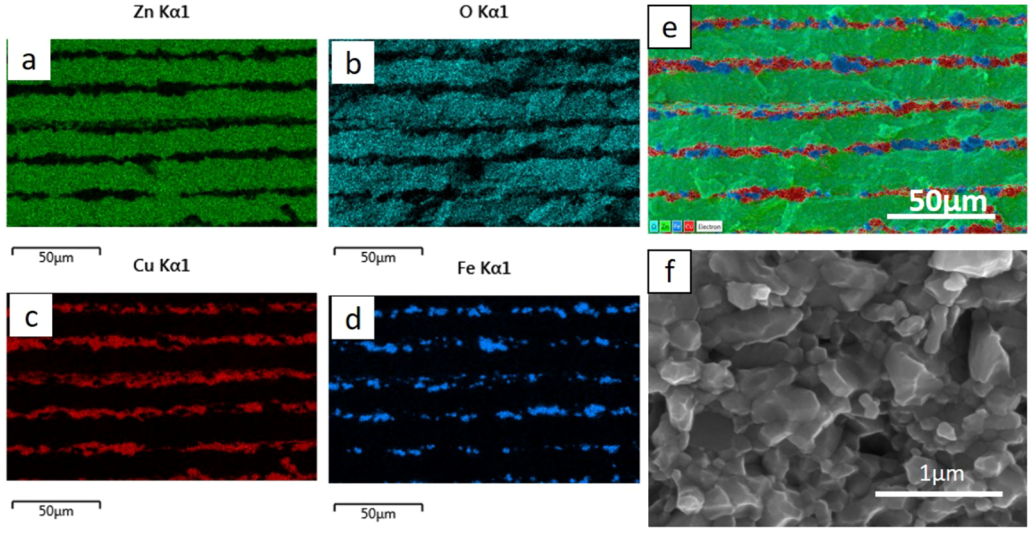

Figure 6. (a–d) SEM–EDX mapping of Zn, O, Cu and Fe elements, (e) resulting EDS mapping, and (f) ZnO phase microstructure of a sample prepared from an ink containing 75 vol % of Cu and 25 vol % of Fe.

layers, at least within the micrometer length scale resolution given by the probe size. Collectively, these observations confirm the quality of sintering and the feasibility of the cold sintering process, in allowing the production of multilayer device with dense microstructures and architectures, with different materials, independent of their relative nature, thermal stability, or chemical compatibility.

We have also found it possible to prepare pastes containing a mixture of two metal powder chemistries to use composite metal electrode for screen printing. Therefore, we could produce multilayers with electrodes containing a mix of Fe and Cu powders, as shown in Figure 6. This example contains a Fe/Cu ratio of 0.25 by volume fraction.

To investigate the nanoscale interface chemistry of metal–metal and metal–ceramic grains, STEM was performed on

DOI: 10.1021/acsaelm.9b00184
ACS Appl. Electron. Mater. 2019, 1, 1198–1207

samples, and chemical mapping was utilized. Figure 7a–e displays typical multilayer ZnO–Cu samples at the interface between some ZnO grains (top) and a Cu grain (bottom). As confirmed from the EDS and STEM images, there is no diffusion between the adjacent layers, even at the nanometer level. It is clear no contamination arises during the process, and there is no interdiffusion or interphase formation. Another important observation is that there is no evidence even at the nanoscale for the oxidation of copper from these STEM mapping images. As was already indicated, at a temperature of even 200 °C, the oxidation can easily[57] occur in an air atmosphere. Thus, the debinding atmosphere is crucial when working with atmosphere sensitive metal electrode, even these at very low temperatures. Thus, our strategy is to use H_2(5 vol %)/N_2(95 vol %) forming a gas atmosphere to prevent any oxidation of copper. The multilayer ZnO–Cu sample XRD data of after debinding can be seen in Figure S1.

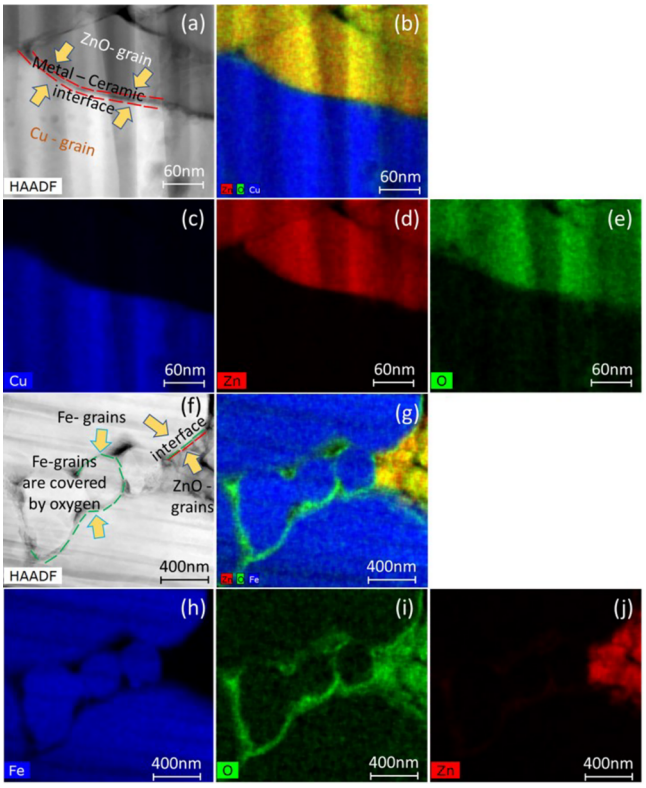

Figure 7. STEM-EDS images of two samples: (a–e) ZnO–Cu and (f–j) ZnO–Fe showing elements location at the interfaces between ZnO and metal.

Figure 7f–g also shows the results from the multilayer ZnO–Fe sample. These images confirm the formation of necks between Fe grains during sintering (visible in Figure 7f); there is also the presence of an oxide nanoscale layer on the Fe grains. As already reported, an oxide layer can form on iron particles at temperatures of 260 and 400 °C in dry and humid atmosphere conditions, forming an oxide layer of 200 nm at 260 °C after 95 h.[59] This result is consistent with the observations of grains having oxide thicknesses ranging from 10 to 100 nm. The oxidation is driven by O_2, H_2O (molecular), and acetic acid, all available under the cold sintering conditions. In conventional LTCC process the interdiffusion of metals in a ceramics matrix plays an essential role in cofired multilayer ceramics. The process is exposed as two firing steps: the binder burnout, which normally take place at around at 500 and 600 °C to remove organics, and the cofiring of ceramic and metallic phase which occurs above 850–1050 °C. There are many studies reporting interdiffusion taking place during firing because the sintering temperature is very close to the melting temperature of metals, especially when cofiring with Ag and Cu, which have melting points of 961 and 1084 °C, respectively.[31,65,66] Here, by use of the cold sintering, the LTCC processing is performed at extremely low temperatures below 300 °C, which well below the melting points of Cu, Fe, and Al metals that are used as a metal layers in this study. As depicted in TEM analysis (Figures 7 and 8), the interfaces of ceramic/metal and metal/ceramic are very clear, and no chemical and physical interdiffusions of the adjacent layers are observed. This demonstrates the capability of applying cold sintering to integrate the electrode and ceramic matrix at low temperatures and thereby extend the field of ultralow-temperature cofired ceramic processing.

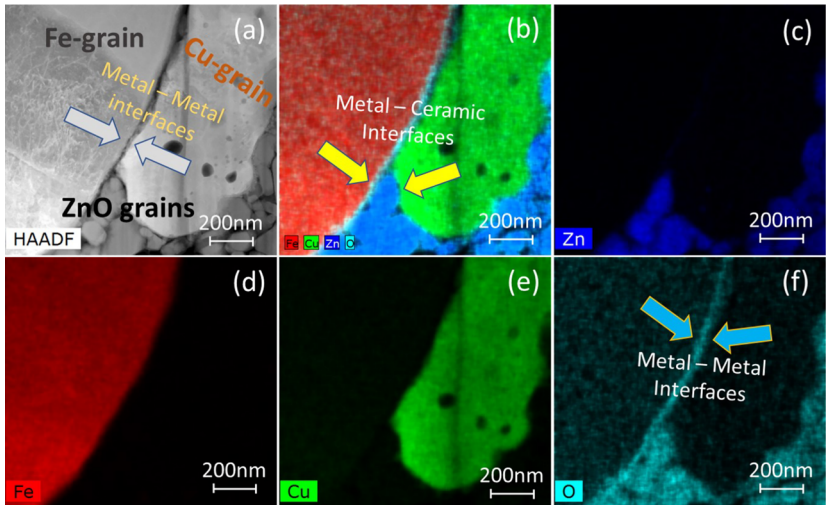

Figure 8. STEM-EDS mapping of ZnO–Cu/Fe volume fraction (50–50) of composite sample (a) microstructure of ZnO with Cu/Fe grains was taken by the high angle annular dark field (HAADF) detector and (b–f) showing cationic and oxygen positions at the interface.

DOI: 10.1021/acsaelm.9b00184
ACS Appl. Electron. Mater. 2019, 1, 1198–1207

In the case of the mixed composite electrode (Figure 7), the Cu surface remains stable, while Fe grains have a surface oxidation, as seen previously in the pure systems. Oxidation of the Fe relative to the Cu is to be expected, given the heat of oxidation and the reactivity series that are well-known and listed in metals (Tables S1 and S2). It is also important to note the lack of a carbon signature in the STEM EDS analysis (Figures 7 and 8), indicating no residual carbon at the interface or grain boundaries after sintering. This indicates that a clean BBO was performed in the H_2/N_2 atmosphere with the propylene carbonate-based binder system.

The all-important property of electrical conductivity can be accessed via electric sheet resistance. Electric sheet resistance (ESR or surface resistance) is a convenient characterization technique that is used for the electrical properties of thin films or thick metal sheet surfaces that are >1000 Å.[67] Although the cofired multilayer samples with Cu, Fe, and Al base metals were all sintered under the same conditions, the samples also were exposed to two different debinding atmospheres of N_2 and H_2 (5 vol %)/N_2(95 vol %). It can be shown that from Table 2 the BBO atmosphere strongly influences the electrical sheet resistance via the oxidizing of metal. The multilayer samples cofired with Fe and Al metals exhibit a very high sheet resistance when using N_2 gas atmosphere in the debinding stage (Table 2), which is clearly due to an extensive oxidation at the grain surfaces. When binder removal take place under a H_2/N_2 forming gas, the ESR for Al electrode was greatly improved, obtaining an ESR ~ 2.3×10^4 mΩ/sq. This value agrees with the ESR ~ 2.4×10^3 mΩ/sq of Al thin film, which were deposited by physical vapor deposition.[68]

Table 2. Comparison of the Electric Sheet Resistance of Cu, Fe, and Al Metal Sheets of Cofired Multilayers

binder burnout atmosphere	sintering atmosphere	ESR of metal sheets (mΩ/sq)		
		Cu	Fe	Al
N_2	in die (ambient)	210	3.6×10^4	1.1×10^7
H_2(5 vol %)/ N_2(95 vol %)	in die (ambient)	6.50	114	2.3×10^4

Generally, if we control the atmosphere in the binder burnout process for the metals Fe, Al, and Cu and then apply the cold sintering process, excellent conductivities can be obtained. As seen from Table 2, the Cu layer has a sheet resistance of 6.50 mΩ/sq, while the Fe metal layer presents a sheet resistance of 114 mΩ/sq. To put these measurements in context, Table S3 reveals many studies reported for deposition and/or traditional thick film, and we see that the cold sintering ESR is highly comparable with the reported data.

Figure 9 shows the trends and variability of sheet resistance behaviors of Cu/Fe mixed metal composite cosintered with ZnO as a function of volume fractions of Fe powders. The figure also shows the schematics of the Cu and Fe metals that are cold sintered in the electrode layers. We proposed this schematic representation of ferroic oxide from TEM images, where it can be shown (Figure 7) that the Fe metal grains are covered by oxygen layer. As previously mentioned, the oxygen layer thickness was determined to be in the nanometers range. The property trends in diphasic composites can be phenomenologically modeled with the rule of mixtures that weight the averaged values of resistivity from the lowest to the highest and the connectivity that weighs the parallel and series contributions. As the volume fraction of the most resistive increases, it will be most impacted around the critical percolation volume fractions.[69] The laws of mixture assume that there are no chemical reactions that influence the trends. In this specific case, we know that there is a chemical interaction via an oxidation of the Fe particles, and this would not be a problem provided that the thickness of that oxidation layer was constant though all the volume fractions and represented the oxidation of the pure Fe end member. As the

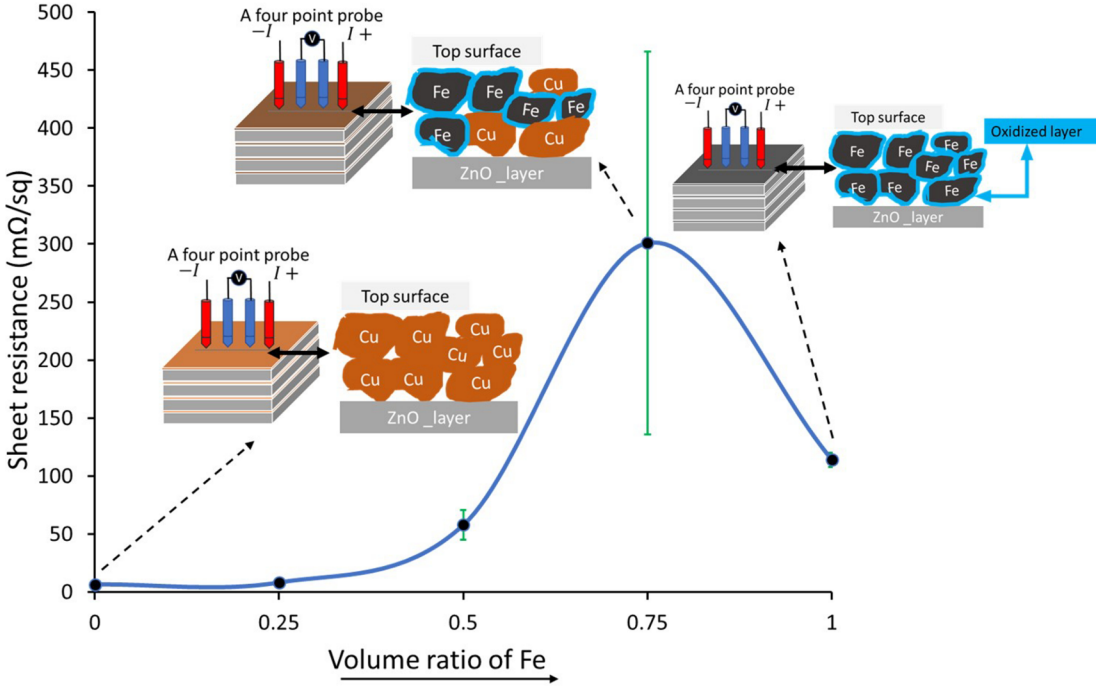

Figure 9. ESR measurements for ZnO−Fe/Cu samples with different metallic volume ratio.

DOI: 10.1021/acsaelm.9b00184
ACS Appl. Electron. Mater. 2019, 1, 1198−1207

ESR has a maximum, this simple assumption does not hold, and there is therefore a population of Fe particles that have thicker oxidation layers under the process and thereby creates a peak in ESR. The standard deviation is also greater in this volume fraction range, indicating that reproducibility is difficult to control with the oxidation kinetics also influencing the highly sensitive regions near the percolation limits. When there is an increase in the oxidation thick film around the grain boundary, this limits the conduction across the interfaces. When the volume fraction of iron is at <0.5 vol % at the composite, the pure Cu metal grains connected with each other, avoiding the resistive pathways of the Fe and Fe-oxide layers. The sheet resistivity anomaly is at the 0.75 vol % of Fe; pure Cu metal grains meet more oxidized Fe phase, and the resistivity reaches the highest point of the Cu−Fe metal−metal composite system due to the breaking up between Cu metal network by the more oxidized Fe phase.[70]

CONCLUSIONS

A very important aspect of forming functional electroceramics is the integration of metallization in a cofiring process with the electroceramic material. Here we have determined the ability to cold sinter metal and coprocess these into highly conductive layers in a multilayer form. Specifically, we demonstrate this by the prototyping of multilayered devices involving an oxide layer (ZnO) and a metallic layer (e.g., Cu, Fe, and Al). An important part of this is forming and removing polymers at low temperatures. We have developed tapes and thick film formulations based on polypropylene carbonate polymers (QPAC) that under forming gases decomposition of the polymer binder make it possible to be removed below 200 °C and control the oxidation of metals such as Cu, Fe, and Al. The metals could be densified and produce high conduction, as quantified from a four-point measurement of the ESR, and these compare extremely well with literature values. The ceramic−metal interfaces show no porosity or interdiffusion issues between the ZnO/metal interfaces. The highest performance conductivity is with the Cu electrodes. In mixing Cu and Fe powders to form composite electrodes, we have seen that there is surface nanoscale oxidation (~10 nm) on the Fe, and this, combined with the percolation, increases the standard deviation of the ESR.

The ability for the cosintering of metals and ceramics under a cold sintering opens new opportunities to form a broader group of materials, known as cermets, as well as the multilayer formats that were the focus of this investigation.

ASSOCIATED CONTENT

Supporting Information

The Supporting Information is available free of charge on the ACS Publications website at DOI: 10.1021/acsaelm.9b00184.

Schematic representation of XRD on the multilayer samples (Figure S1); XRD data of the multilayer device with Al, Cu, and Fe powders were performed after binder burnout (Figure S2); XRD data of the multilayer device of the Al, Cu, and Fe metals were performed after cold sintering (Figure S3); activity series of metals and their oxidation reaction and energy data (Table S1); heat of oxidation for potential electrode chemistries (Table S2); comparison of the ESR of different metal type reported for deposition and/or traditional thick film (Table S3) (PDF)

AUTHOR INFORMATION

Corresponding Author

*(S.D.) E-mail: sxd448@psu.edu.

ORCID

Sinan Dursun: 0000-0001-9270-3368

Notes

The authors declare no competing financial interest.

ACKNOWLEDGMENTS

This material is based upon work supported by the National Science Foundation, as part of the Center for Dielectrics and Piezoelectrics under Grants IIP-1361571 and 1361503. We thank Shoei Chemical for supplying copper powders and Empower Materials for supplying binder polymers. Any opinions, findings, conclusions, or recommendations expressed in this material are those of the author(s) and do not necessarily reflect the views of the Foundation. The authors acknowledge Amanda Baker, Steve Perini, Jeff Long, Julie Anderson, and Ke Wang for their technical support during this study and Joanne Aller for editorial contributions.

REFERENCES

(1) Kishi, H.; Mizuno, Y.; Chazono, H. Base-Metal Electrode-Multilayer Ceramic Capacitors: Past, Present and Future Perspectives. *Japanese J. Appl. Physics, Part 1 Regul. Pap. Short Notes Rev. Pap.* **2003**, *42* (1), 1−5.

(2) Lee, K.-H.; Wu, Y.-C.; Lu, H.-Y. Interface Microstructure between Ni Base-Metal Electrode and $BaTiO_3$ Dielectric. *J. Phys. D: Appl. Phys.* **2007**, *40* (16), 4902−4909.

(3) Zhou, D.; Chen, Y.; Zhang, D.; Liu, H.; Hu, Y.; Gong, S. Fabrication and Characterization of the Multilayered PTCR Ceramic Thermistors by Slip Casting. *Sens. Actuators, A* **2004**, *116* (3), 450−454.

(4) Feteira, A. Negative Temperature Coefficient Resistance (NTCR) Ceramic Thermistors: An Industrial Perspective. *J. Am. Ceram. Soc.* **2009**, *92* (5), 967−983.

(5) Töpfer, J.; Mürbe, J.; Angermann, A.; Kracunovska, S.; Barth, S.; Bechtold, F. Soft Ferrite Materials for Multilayer Inductors. *Int. J. Appl. Ceram. Technol.* **2006**, *3* (6), 455−462.

(6) Buschow, K. H. J. *Encyclopedia of Materials: Science and Technology*; Elsevier: 2001.

(7) Uchino, K.; Takahashi, S. Multilayer Ceramic Actuators. *Curr. Opin. Solid State Mater. Sci.* **1996**, *1* (5), 698−705.

(8) Zheng, J.; Takahashi, S.; Yoshikawa, S.; Uchino, K.; de Vries, J. W. C. Heat Generation in Multilayer Piezoelectric Actuators. *J. Am. Ceram. Soc.* **1996**, *79* (12), 3193−3198.

(9) Randall, C. A.; Kelnberger, A.; Yang, G. Y.; Eitel, R. E.; Shrout, T. R. High Strain Piezoelectric Multilayer Actuators:A Material Science and Engineering Challenge. *J. Electroceram.* **2005**, *14* (3), 177−191.

(10) Shebanovs, L.; Borman, K.; Lawless, W. N.; Kalvane, A. Electrocaloric Effect in Some Perovskite Ferroelectric Ceramics and Multilayer Capacitors. *Ferroelectrics* **2002**, *273* (1), 137−142.

(11) Qian, X.-S.; Ye, H.-J.; Zhang, Y.-T.; Gu, H.; Li, X.; Randall, C. A.; Zhang, Q. M. Giant Electrocaloric Response Over A Broad Temperature Range in Modified $BaTiO_3$ Ceramics. *Adv. Funct. Mater.* **2014**, *24* (9), 1300−1305.

(12) Kerman, K.; Luntz, A.; Viswanathan, V.; Chiang, Y.-M.; Chen, Z. Review—Practical Challenges Hindering the Development of Solid State Li Ion Batteries. *J. Electrochem. Soc.* **2017**, *164* (7), A1731−A1744.

(13) Liu, W.; Milcarek, R. J.; Falkenstein-Smith, R. L.; Ahn, J. Interfacial Impedance Studies of Multilayer Structured Electrolyte Fabricated With Solvent-Casted PEO_{10}-$LiN(CF_3SO_2)_2$ and Ceramic $Li_{1.3}Al_{0.3}Ti_{1.7}(PO_4)_3$ and Its Application in All-Solid-State Lithium Ion Batteries. *J. Electrochem. Energy Convers. Storage* **2016**, *13* (2), 021008.

DOI: 10.1021/acsaelm.9b00184
ACS Appl. Electron. Mater. 2019, 1, 1198−1207

(14) Jantunen, H.; Kangasvieri, T.; Vähäkangas, J.; Leppävuori, S. Design Aspects of Microwave Components with LTCC Technique. *J. Eur. Ceram. Soc.* **2003**, *23* (14), 2541−2548.
(15) Golonka, L.; Bembnowicz, P.Ł; Jurków, D.; Malecha, K.; Roguszczak, H.; Tadaszak, R. *Low Temperature Co-Fired Ceramics (LTCC) Microsystems.* **2011**, *XLI* (2), 383−388.
(16) Töpfer, J.; Reimann, T.; Schulz, T.; Bochmann, A.; Capraro, B.; Barth, S.; Vogel, A.; Teichert, S. Oxide Multilayer Thermoelectric Generators. *Int. J. Appl. Ceram. Technol.* **2018**, *15* (3), 716−722.
(17) Funahashi, S.; Nakamura, T.; Kageyama, K.; Ieki, H. Monolithic Oxide-metal Composite Thermoelectric Generators for Energy Harvesting. *J. Appl. Phys.* **2011**, *109* (12), 124509.
(18) Yao, L.; Ou, G.; Liu, W.; Zhao, X.; Nishijima, H.; Pan, W. Fabrication of High Performance Oxygen Sensors Using Multilayer Oxides with High Interfacial Conductivity. *J. Mater. Chem. A* **2016**, *4* (29), 11422−11429.
(19) Müller, A. C.; Herbstritt, D.; Ivers-Tiffée, E. Development of a Multilayer Anode for Solid Oxide Fuel Cells. *Solid State Ionics* **2002**, *152−153*, 537−542.
(20) Pan, M.-J.; Randall, C. A. A Brief Introduction to Ceramic Capacitors. *IEEE Electr. Insul. Mag.* **2010**, *26* (3), 44−50.
(21) Shanefield, D. J. *Organic Additives and Ceramic Processing: With Applications in Powder Metallurgy, Ink, and Paint*; Springer: New York, 1995.
(22) Imanaka, Y. *Multilayered Low Temperature Cofired Ceramics (LTCC) Technology*; Kluwer Academic Publishers: Boston, 2005.
(23) Polotai, A. V.; Fujii, I.; Shay, D. P.; Yang, G.-Y.; Dickey, E. C.; Randall, C. A. Effect of Heating Rates during Sintering on the Electrical Properties of Ultra-Thin NiBaTiO $_3$ Multilayer Ceramic Capacitors. *J. Am. Ceram. Soc.* **2008**, *91* (8), 2540−2544.
(24) Yang, G. Y.; Lee, S. I.; Liu, Z. J.; Anthony, C. J.; Dickey, E. C.; Liu, Z. K.; Randall, C. A. Effect of Local Oxygen Activity on Ni-$BaTiO_3$ Interfacial Reactions. *Acta Mater.* **2006**, *54* (13), 3513−3523.
(25) Kumar, N.; Ionin, A.; Ansell, T.; Kwon, S.; Hackenberger, W.; Cann, D. Multilayer Ceramic Capacitors Based on Relaxor $BaTiO_3$-$Bi(Zn_{1/2}Ti_{1/2})O_3$ for Temperature Stable and High Energy Density Capacitor Applications. *Appl. Phys. Lett.* **2015**, *106* (25), 252901.
(26) Shay, D. P.; Podraza, N. J.; Donnelly, N. J.; Randall, C. A. High Energy Density, High Temperature Capacitors Utilizing Mn-Doped $0.8CaTiO_3$-$0.2CaHfO_3$ Ceramics. *J. Am. Ceram. Soc.* **2012**, *95* (4), 1348−1355.
(27) Shimada, T.; Touji, K.; Katsuyama, Y.; Takeda, H.; Shiosaki, T. Lead Free PTCR Ceramics and its Electrical Properties. *J. Eur. Ceram. Soc.* **2007**, *27* (13−15), 3877−3882.
(28) Cann, D. P.; Randall, C. A. Electrode Effects in Positive Temperature Coefficient and Negative Temperature Coefficient Devices Measured by Complex-plane Impedance Analysis. *J. Appl. Phys.* **1996**, *80* (3), 1628−1632.
(29) Kawada, S.; Kimura, M.; Higuchi, Y.; Takagi, H. (K,Na)NbO $_3$ -Based Multilayer Piezoelectric Ceramics with Nickel Inner Electrodes. *Appl. Phys. Express* **2009**, *2* (11), 111401.
(30) Kobayashi, K.; Doshida, Y.; Mizuno, Y.; Randall, C. A. Possibility of Cofiring a Nickel Inner Electrode in a $(Na_{0.5}K_{0.5})NbO_3$ -LiF Piezoelectric Actuator. *Jpn. J. Appl. Phys.* **2013**, *52* (9S1), 09KD07.
(31) Gao, L.; Ko, S.-W.; Guo, H.; Hennig, E.; Randall, C. A. Demonstration of Copper Co-Fired (Na, K)NbO_3 Multilayer Structures for Piezoelectric Applications. *J. Am. Ceram. Soc.* **2016**, *99* (6), 2017−2023.
(32) Jiang, X. P.; Liao, J.; Zhang, W. Z.; Li, G. R.; Ying, Q. R. PZN-PZT Piezoelectric Multilayer Actuator with Ag/Pd Electrodes. *J. Materials Sci. Technol.* **2000**, *16*, 421−423.
(33) Donnelly, N. J.; Randall, C. A. Refined Model of Electromigration of Ag/Pd Electrodes in Multilayer PZT Ceramics Under Extreme Humidity. *J. Am. Ceram. Soc.* **2009**, *92* (2), 405−410.
(34) Donnelly, N. J.; Shrout, T. R.; Randall, C. A.; Reaney, I. M. Thermochemical Reactions Between PZT and Ag/Pd Powders: Relevance to Cofiring of Multilayer Actuators. *J. Am. Ceram. Soc.* **2008**, *91* (3), 1013−1018.
(35) Gao, Z.; Sun, H.; Fu, L.; Ye, F.; Zhang, Y.; Luo, W.; Huang, Y. Promises, Challenges, and Recent Progress of Inorganic Solid-State Electrolytes for All-Solid-State Lithium Batteries. *Adv. Mater.* **2018**, *30* (17), 1705702.
(36) Wang, Y.; Zhang, G.; Ma, J. Research of LTCC/Cu, Ag Multilayer Substrate in Microelectronic Packaging. *Mater. Sci. Eng., B* **2002**, *94* (1), 48−53.
(37) Kwon, D.-K.; Lanagan, M. T.; Shrout, T. R. Microwave Dielectric Properties and Low-Temperature Cofiring of $BaTe_4O_9$ with Aluminum Metal Electrode. *J. Am. Ceram. Soc.* **2005**, *88* (12), 3419−3422.
(38) Ramamoorthy, R.; Dutta, P. K.; Akbar, S. A. Oxygen Sensors: Materials, Methods, Designs and Applications. *J. Mater. Sci.* **2003**, *38* (21), 4271−4282.
(39) Lee, Y.-S.; Tseng, T.-Y. Influence of Processing Parameters on the Microstructure and Electrical Properties of Multilayer-Chip ZnO Varistors. *J. Mater. Sci. Mater. Electron.* **1995**, *6* (2), 90−96.
(40) Cologna, M.; Contino, A. R.; Sglavo, V. M.; Modena, S.; Ceschini, S.; Bertoldi, M. *Curvature Evolution and Control in Anode Supported Solid Oxide Fuel Cells*; John Wiley & Sons, Ltd.: 2010; pp 95−104.
(41) Green, D. J.; Guillon, O.; Rödel, J. Constrained Sintering: A Delicate Balance of Scales. *J. Eur. Ceram. Soc.* **2008**, *28* (7), 1451−1466.
(42) Chiang, M.-J.; Jean, J.-H.; Lin, S.-C. Effects of Green Density Difference on Camber Development during the Cofiring of a Bi-Layer Glass-Based Dielectric Laminate. *Mater. Chem. Phys.* **2011**, *128* (3), 413−417.
(43) Hsu, R.-T.; Jean, J.-H. Key Factors Controlling Camber Behavior During the Cofiring of Bi-Layer Ceramic Dielectric Laminates. *J. Am. Ceram. Soc.* **2005**, *88* (9), 2429−2434.
(44) Cai, P. Z.; Green, D. J.; Messing, G. L. Constrained Densification of Alumina/Zirconia Hybrid Laminates, I: Experimental Observations of Processing Defects. *J. Am. Ceram. Soc.* **1997**, *80* (8), 1929−1939.
(45) Brillson, L. J. Transition in Schottky Barrier Formation with Chemical Reactivity. *Phys. Rev. Lett.* **1978**, *40* (4), 260−263.
(46) Black, J. R. *Proceedings of the 6th Annual Reliability Physcis Symposium*; IEEE: New York, 1967.
(47) Wang, S. F.; Dougherty, J. P.; Huebner, W.; Pepin, J. G. Silver-Palladium Thick-Film Conductors. *J. Am. Ceram. Soc.* **1994**, *77* (12), 3051−3072.
(48) Cann, D. P.; Randall, C. A. The Thermochemistry and Non-Ohmic Electrical Contacts of a $BaTiO_3$ PTCR Ceramic. *IEEE Trans. Ultrason. Ferroelectr. Freq. Control* **1997**, *44* (6), 1405−1408.
(49) Guo, J.; Guo, H.; Baker, A. L.; Lanagan, M. T.; Kupp, E. R.; Messing, G. L.; Randall, C. A. Cold Sintering: A Paradigm Shift for Processing and Integration of Ceramics. *Angew. Chem., Int. Ed.* **2016**, *55* (38), 11457−11461.
(50) Guo, J.; Baker, A. L.; Guo, H.; Lanagan, M.; Randall, C. A. Cold Sintering Process: A New Era for Ceramic Packaging and Microwave Device Development. *J. Am. Ceram. Soc.* **2017**, *100* (2), 669−677.
(51) Guo, H.; Baker, A.; Guo, J.; Randall, C. A. Cold Sintering Process: A Novel Technique for Low-Temperature Ceramic Processing of Ferroelectrics. *J. Am. Ceram. Soc.* **2016**, *99* (11), 3489−3507.
(52) Guo, J.; Berbano, S. S.; Guo, H.; Baker, A. L.; Lanagan, M. T.; Randall, C. A. Cold Sintering Process of Composites: Bridging the Processing Temperature Gap of Ceramic and Polymer Materials. *Adv. Funct. Mater.* **2016**, *26* (39), 7115−7121.
(53) Funahashi, S.; Guo, H.; Guo, J.; Baker, A. L.; Wang, K.; Shiratsuyu, K.; Randall, C. A. Cold Sintering and Co-Firing of a Multilayer Device with Thermoelectric Materials. *J. Am. Ceram. Soc.* **2017**, *100* (8), 3488−3496.
(54) Seo, J.-H.; Verlinde, K.; Guo, J.; Heidary, D. S. B.; Rajagopalan, R.; Mallouk, T. E.; Randall, C. A. Cold Sintering Approach to Fabrication of High Rate Performance Binderless $LiFePO_4$ Cathode with High Volumetric Capacity. *Scr. Mater.* **2018**, *146*, 267−271.
(55) Smits, F. M. *Bell Syst. Technol. J.* **1958**, *37*, 711−718.

DOI: 10.1021/acsaelm.9b00184
ACS Appl. Electron. Mater. 2019, 1, 1198−1207

(56) Lee, S.-K.; Hsu, H.-C.; Tuan, W.-H. Oxidation Behavior of Copper at a Temperature below 300 °C and the Methodology for Passivation. *Mater. Res.* **2016**, *19* (1), 51−56.
(57) Roosendaal, S. J.; Vredenberg, A. M.; Habraken, F. H. P. M. Oxidation of Iron: The Relation between Oxidation Kinetics and Oxide Electronic Structure. *Phys. Rev. Lett.* **2000**, *84* (15), 3366−3369.
(58) Pranda, P.; Prandová, K.; Hlavacek, V. Particle Size and Reactivity of Aluminum Powders. *Combust. Sci. Technol.* **2000**, *156* (1), 81−96.
(59) Bertrand, N.; Desgranges, C.; Poquillon, D.; Lafont, M. C.; Monceau, D. Iron Oxidation at Low Temperature (260−500 °C) in Air and the Effect of Water Vapor. *Oxid. Met.* **2010**, *73* (1−2), 139−162.
(60) Lewis, J. A. Binder removal from ceramics. *Annu. Rev. Mater. Sci.* **1997**, *27* (1), 147−173.
(61) German, R. M. Theory of Thermal Debinding. *Int. J. Powder Metall.* **1987**, *23*, 237−245.
(62) Empower Materials, Inc. QPAC®40 TGA versus PVB and Ethyl Cellulose binders; http://empowermaterials.com/wp-content/uploads/2017/07/QPAC40-TGA-comparison-with-PVB-Ethyl-Cellulose-binders.pdf (accessed May 22, 2019).
(63) Empower Materials, Inc. Poly(Alkylene Carbonates) as Binder in Electronic Component Manufacturing Applications. QPAC®40 TGA versus PVB and Ethyl Cellulose binders; http://empowermaterials.com/wp-content/uploads/2017/07/QPAC40-TGA-Results-in-Various-Environments.pdf (accessed May 22, 2019).
(64) Gao, L.; Guo, H.; Zhang, S.; Randall, A. C. Base Metal Co-Fired Multilayer Piezoelectrics. *Actuators* **2016**, *5* (1), 8.
(65) Lee, W. H.; Su, C. Y. Characterization of silver interdiffusion into (Zn,Mg)TiO_{3+x}:Bi:Sb Multilayer Ceramic Capacitor. *J. Am. Ceram. Soc.* **2007**, *90* (8), 2454−2460.
(66) Lee, Y. P.; et al. Interdiffusion in Pd/Cu Multilayered Film. *Mater. Sci. Forum* **1995**, *189−190*, 411−416.
(67) Ghosh, D. S. *Basics of Ultrathin Metal Films and Their Use as Transparent Electrodes*; Springer: Heidelberg, 2013; pp 11−32.
(68) Panta, G.; Subedi, D. Electrical Characterization of Aluminum (Al) Thin Films Measured by Using Four- Point Probe Method. *Kathmandu Univ. J. Sci. Eng. Technol.* **2013**, *8* (2), 31−36.
(69) Zhang, W.; Brongersma, S. H.; Clarysse, T.; Terzieva, V.; Rosseel, E.; Vandervorst, W.; Maex, K. Surface and Grain Boundary Scattering Studied in Beveled Polycrystalline Thin Copper Films. *J. Vac. Sci. Technol., B: Microelectron. Process. Phenom.* **2004**, *22* (4), 1830.
(70) Nan, C.-W.; Shen, Y.; Ma, J. Physical Properties of Composites Near Percolation. *Annu. Rev. Mater. Res.* **2010**, *40* (1), 131−151.

DOI: 10.1021/acsaelm.9b00184
ACS Appl. Electron. Mater. 2019, 1, 1198−1207